



# Analysis of Contact Stress and Fatigue Crack Growth of Transmission Shaft

Long Li · Tianxiang Yu · Bolin Shang · Bifeng Song · Yijian Chen

Submitted: 21 October 2022 / in revised form: 26 December 2022 / Accepted: 5 January 2023 / Published online: 20 January 2023  
© ASM International 2023

**Abstract** The finite element model and fracture mechanic theory are applied to analyze the contact stress and fatigue crack growth (FCG) path in three dimensions for a transmission shaft, which owns the initial crack and runs with the periodic load. The study found that the periodic load generates a non-proportional stress intensity factor history (SIF) output in the root of the splines. A modified method based on Hertz theory and AGMA (American Gear Manufacture Association) standard is utilized to analyze contact stress with considering the crack growth. From this, it is feasible to predict FCG path in three dimensions for a cracked component. The comparison between the simulation and experiment illustrates that the crack growth path is sensitive to the location and magnitude of loads. Contact regions of stress and fracture mechanic parameters should be deeply analyzed and known before predicting FCG path in three dimensions.

**Keywords** Contact stress · Fatigue crack growth · Local finite element model · Transmission shaft

## List of symbols

$T_M$	Main torque (77.51 N*m)
$T_S$	Sub-cycle torque (7.75 N*m)
$T_M/T_S$	Cyclic ratio (1:2667)
$F_{n_i} (i = 1, 2, \dots, 24)$	Normal force on spline surface (N)
$F_{t_i}$	Tangential force on spline surface (N)
$F_{r_i}$	Radial force (N)
$S_i (i = 1, 2, \dots, 9)$	Different stages of the FCG test

$\sigma_x, \sigma_y$	Stress of crack front on the x-axis and y-axis (MPa)
$\Delta K_i (i = I, II)$	Magnitude of $K_I$ and $K_{II}$
$\sigma_\theta$	Circumference stress (MPa)
$\alpha_i (i = 1, \dots, 9)$	Offset angle from contact stress to initial tangential force (degree)
$\theta$	Crack growth angle (radian)
$da_i$	Increment of crack length
$dN_i$	Increment of cyclic times
$a_x, a_y$	Semimajor and semiminor axes of the crack (mm)
$r$	Radius of torque
$T_N$	Teeth count of interior splines
$C, m$	Material constant
$\Delta K_{eq}$	Magnitude of equivalent SIF

## Introduction

A transmission shaft is widely used to transfer power in the engine system. Because of cyclic loads or sudden impact, the transmission shaft may encounter fracture failure caused by a fatigue crack, which often appears in the stress concentration areas. The crack not only changes the contact stress between transmission shaft splines but increases the difficulties to predict the remaining FCG path. Indeed, contact stress is crucial information to evaluate the health status of splines. However, it is hard to calculate due to cracked components having complex three-dimensional geometry and assembly relationship. The focus of this paper is contact stress analysis and FCG path prediction caused by stress fatigue. Stress fatigue often leads to crack initiation and growth from the spline root of the loaded side of the transmission shaft.

L. Li (✉) · T. Yu · B. Shang · B. Song · Y. Chen  
School of Aeronautics, Northwestern Polytechnical University,  
Xi'an, China  
e-mail: leedragon@mail.nwpu.edu.cn

During the daily maintenance of the transmission shaft, cracks are the most probably to be monitored before the fracture failure takes place because of abnormal vibration, change of stress magnitude, or noise frequency, and their growth paths and lengths determine whether the failure is gradual or catastrophic. Motivated by the fracture failure in aerospace and automotive industries [1], lots of results have been paid to contact stress [2, 3], and FCG research. Wu [4] proposed a contact stress analysis approach for the loaded tooth of skew conical involute gear that drives with approximate line contact. Vukelic [5] built a 3D numerical model and performed a finite element stress analysis to research the failure process of the gear shaft. Medvedev [6] constructed a mathematical model and algorithm to analyze the contact stress for multi-pair contact gears. Based on Hertz theory, Perez [7] proposed a contact stress analytical method for gear drives with localized bearing contact. Through the investigation of contact stresses and crack initiation for spur gears, Qin [8] pointed out that friction and speed can affect the stress cycles and fatigue life of gears. Wei [9] made research on the maximum contact stress of spur cylindrical gear. To study the surface failure during the gears meshing, Patil [10] analyzed the contact stress of helical gear pairs considering the change of friction coefficient. Hwang [11] made a contact stress analysis for a pair of mating gears during the rotation, the results show that the contact stress is related to the change of contact position. The research results of Vukelic [12] show the material inclusions and defects below the subsurface are usually the resource of crack initiation, where excessive stress will result in crack growth and contact stress change of gear shafts. Pedrero [13] proposed a new model to deal with the contact stress of gear teeth, considering the load distribution discrepancy along the contact line. Mehta [14] studied the contact stress of mating gears made of composite material.

The FCG path is another crucial character in the fracture failure study of the transmission system, such as mining machine, [15], pump systems [16–18], oil and gas transmission pipelines [19]. Spievak [20] found moving load can generate a non-proportional force in the gear tooth root and gave a path prediction method for the three-dimensional fatigue crack of spiral bevel gear. Fonte [21] studied the influence of steady torsion loading on FCG rates in shafts. Yates [22] summarized the crack path tracking methods and evaluated the stress field strength of mixed modes crack tip by the experimental data. Jiang [23] calculated the local stress of the assembly under torsional load and analyzed the crack propagation with the predicted crack initial position and crack growth routine. Ge [24] studied the fatigue and multiaxial fatigue of the thrust shaft and investigated the crack initiation/strain life. To find how

the gear parameters can affect the crack path and provide help on the gear design to avoid hard failure, Curà [25] researched the crack propagation path in planet gears. Through combining the S-FEM (superposition of finite element meshes) automatic mesh generate technique, Suga [26] developed a model to study the fatigue growth of multi-surface flaws in the shaft under rotary bending. Rubio [27] studied the nonlinear effect of the breathing crack in rotating shaft crack propagation. Based on the XFEM (extended finite element method), Solob [28] analyzed the FCG in the wing-fuselage attachment lug and estimate the residual strength and fatigue life of a cracked component. The model established by Ye [29] can be used to investigate the fatigue crack growth and interaction of multiple surface cracks. By right of constant amplitude loading tests, Dong [30] made research on fatigue crack growth behavior of a corner crack at the edge of a hole, the research results reveal the relationship between the FCG rate and SIF range ( $\Delta K$ ). Langlois et al. [31] designed an experimental benchmark to research the mixed-mode crack propagation and variation of small level yield conditions. By damage tolerant methodology, Fossati [32] investigated the fatigue crack propagation of the damaged transmission shaft. Besides, FCG analysis is also applied in material strength research [33], structure fretting crack propagation prediction [34], and the estimation of residual fatigue life.

Currently, limited studies have paid attention to the contact stress and FCG path prediction of transmission shaft that works with initial crack, a possible reason because it needs a complicated three-dimensional geometry and cracks parameters. Crack length and contact stress, as opposed to the residual life, is key information during the transmission shaft design due to the high stress and use frequency of contact leading to a short period between the crack initiation and fracture failure. Hence, the majority of works are focused on the two-dimensional crack growth path and suppose the contact stress is constant while the component is running. In addition, most studies neglect the dependence of crack growth and contact stress. Consequently, the effects of continuous crack growth on the contact stress of splines and the stress field change of the crack front were not considered during the path prediction. However, the crack growth life (crack initiation and growth stages) has an important application in the health monitoring and reliability evaluation for the engine system. The monitor system can detect or warn the cracks. Subsequently, the drivers and maintainers could be noticed in advance if action needs to be taken to avoid failure.

The purposes of this article are to analyze the contact stress and FCG path of the transmission shaft, in which the initial crack grows along the load cycle times. Different from the existing results, this paper divides the whole FCG

process into a series of discrete growth stages, then, utilizes the local finite element model to replace the global model to simulate the contact stress and FCG of every growth stage. Furthermore, the loading locations and magnitude of the spline change with growth stages are concerned. Compared with the experiment, the simulation verified the sensitivity of contact stress and crack growth path to torque levels and loading locations.

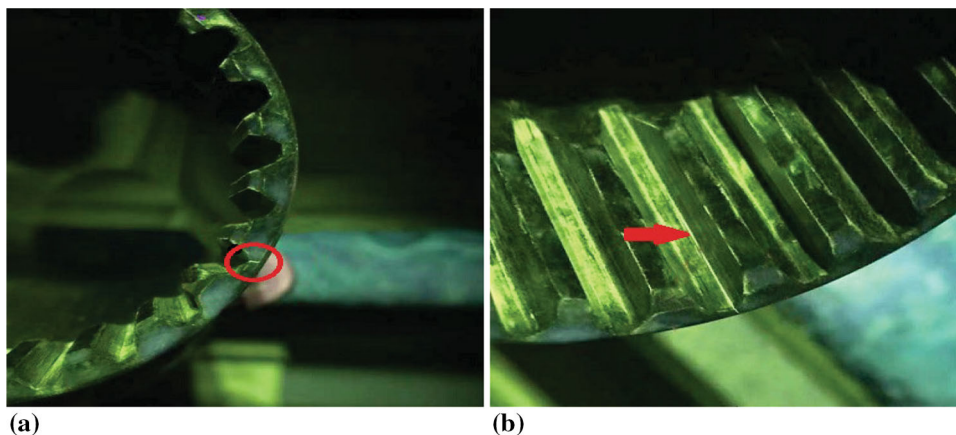
### Background

A transmission shaft and interior spline are shown in Fig. 1. The ordinary inspection found there is a crack in the joint of the spline root and shaft wall, which had grown 1 mm in the radial plane (Fig. 2a) and extends 14.4 mm axially (Fig. 2b). To recognize the contact stress and FCG path of the transmission shaft under practical loading conditions, an FCG experiment was conducted.



Fig. 1 Schematic diagram of transmission shaft and interior spline

Fig. 2 Crack location of the transmission shaft



### Fatigue Crack Growth Experiment

The experiment system and instrument connection are shown in Figs. 3 and 4, respectively. Torques were applied to the flange that connects with the exterior splines, Meanwhile, the crack length was checked every 200 (or

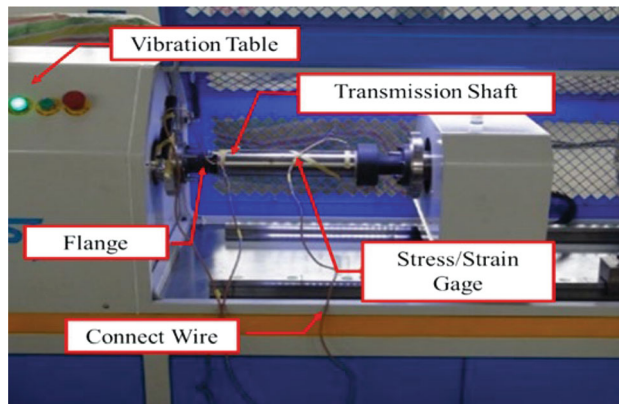
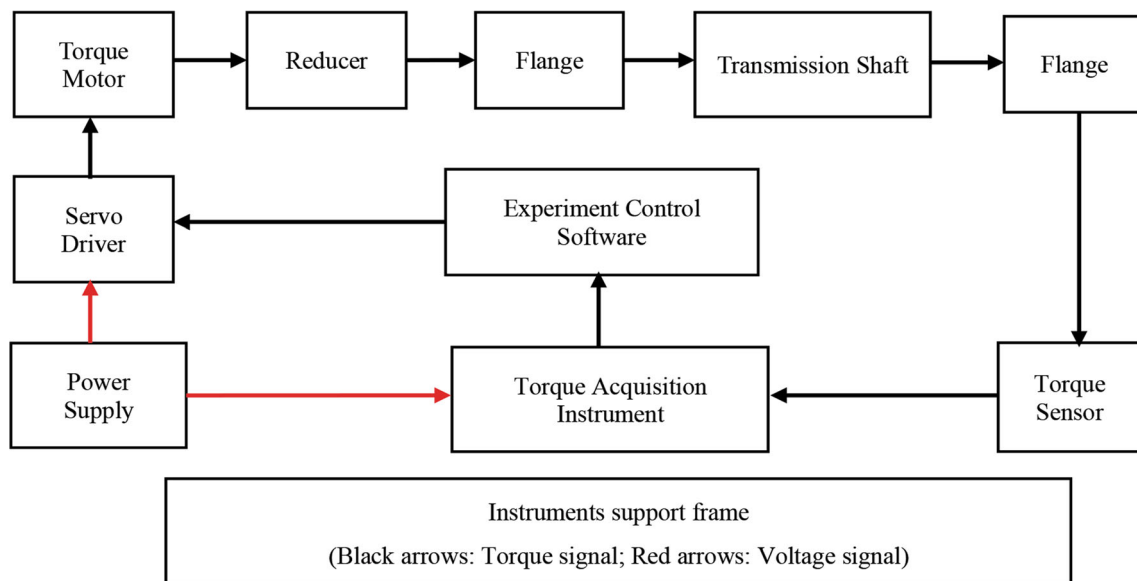
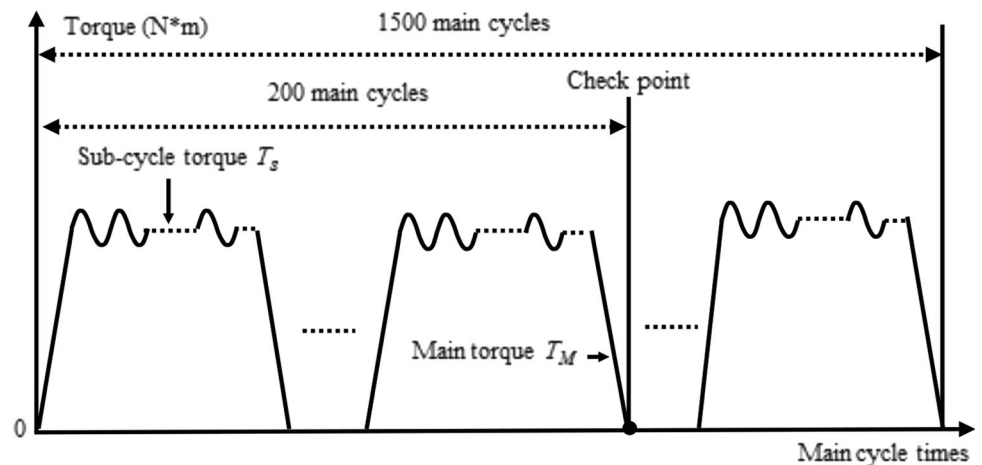


Fig. 3 Diagram of fatigue crack growth experiment



**Fig. 4** Connection schematic of experiment devices

**Fig. 5** Loading process of crack growth experiment of the transmission shaft



100) main cycles until the number of cycles reached 1500. The loading process and flaws of the experiment are illustrated in Figs. 5 and 6.

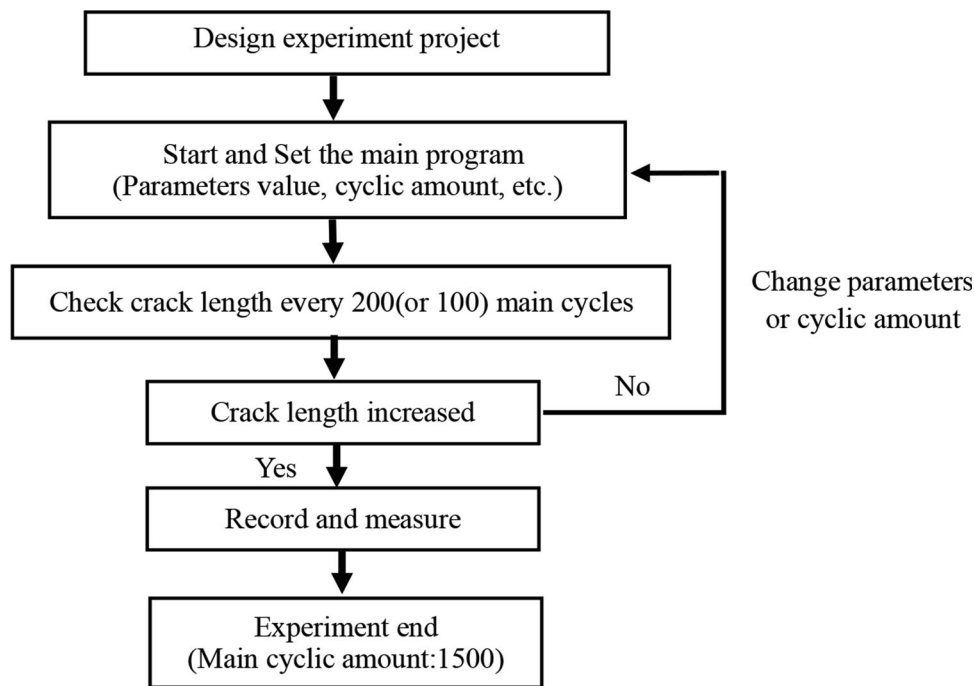
### Experiment Results

The results show radial crack length is invariable, but the axial crack length on the shaft wall surface increases nonlinearly to 14.9 mm and then tends to plateau (Fig. 7). These results suggest that: (1) partial splines may not bear loads or their contact stresses have decreased when the crack grows to a specific length; (2) regarding the contact stress as a constant may not be reasonable during the FCG experiment, indeed, it is a function of main cyclic times,

crack length or pressure angles; (3) crack growth ratio is a variable in different stages. (4) during the 0–14.4 mm growth stages, components of contact stress in radial and axial both take effect in the crack tip, so the crack grows in these two directions, simultaneously. However, in the 14.4–14.9 mm growth stages, there is not enough force component in the radial and therefore, the crack just grows in the axial.

The foregoing analysis illustrates contact stress is crucial information for the loading-bear units, especially when they work with cracks. Contact stress analysis is a valid method to predict the crack growth path and prevent fracture failure occurrences.

**Fig. 6** Simplified flow diagram of fatigue crack experiment



**Analysis of Contact Stress and Crack Growth Path**

**Contact Stress**

In practice, the contact stress and pressure angle between splines can keep stable until a crack appear because a crack can lead to the angles of the stress components changing. Figure 8 is the *x-z* section view in three-dimensional of the local contact relation of flange and spline, it describes the correlation of four parameters that include  $\alpha_i$ ,  $F_{r_i}$ ,  $F_{t_i}$ , and  $S_i$ . When the crack grows,  $F_{r_i}$  and  $F_{t_i}$  will generate  $\sigma_x$  and  $\sigma_y$  in the *x*-axial and *y*-axial at the crack front, respectively.

When the assembly is loaded, there will be tensile stress in the root of loaded sides, and compressive stresses in the contact region between the spline and flange. The contact stress between them may change with teeth depth and, therefore contact stress is remarkable because it can influence the rate and path of crack growth.

As is known, Hertz theory and AGMA standard (“Appendix”) have been applied to calculate the contact stress between units without cracks. However, they cannot be used to analyze the contact stress for cracked structures. This paper developed a new thought of contact stress calculation for the cracked component based on Hertz theory and AGMA standard. For convenience, it is supposed that each growth stage has unique contact stress on the loaded side and the contact region is frictionless, not dynamic.

The relation of initial contact force and force components without crack influence can write as:

$$\begin{cases} F_{t_0} = \frac{T_M + T_S}{T_N r} \\ F_{r_0} = F_{t_0} \times \tan \alpha_0 \\ F_{n_0} = \frac{F_t}{\cos \alpha_0} \end{cases} \quad (\text{Eq 1})$$

Due to the spline and flange being assembled with standard center distance, the pressure angle  $\alpha_0 = 30^\circ$ , so the initial force  $F_{r_0}$ ,  $F_{t_0}$ , and  $F_{n_0}$  can be determined by Eq. 1.  $F_{n_0}$  is perpendicular to the contact line. When a crack appears, the tiny deformation of splines will lead to force components changing from  $F_{n_i}, F_{r_i}, F_{t_i}$  to  $F_{n_{i+1}}, F_{r_{i+1}}, F_{t_{i+1}}$ . The contact stress  $F$  will rotate  $\pm \alpha_i$  from the  $F_{n_i}$ , and it will not be perpendicular to the loaded side, the new force components  $F_{t_1}$  and  $F_{r_1}$  on the tangential and radial directions provide the required growth force of crack front (Fig. 9). Accordingly, every crack growth will generate a new corresponding relation among the force components until the crack growth is stopped.

*Contact Stress of 0–14.4 mm Growth Stage*

Because 0–14.4 mm is the compound crack growth stage, ratio is [35]:

$$\frac{da}{dN} = C(\Delta K_{eq})^m \quad (\text{Eq 2})$$

And,  $\Delta K_{eq}$  is:

**Fig. 7** Relation of axial crack length and main cyclic amount

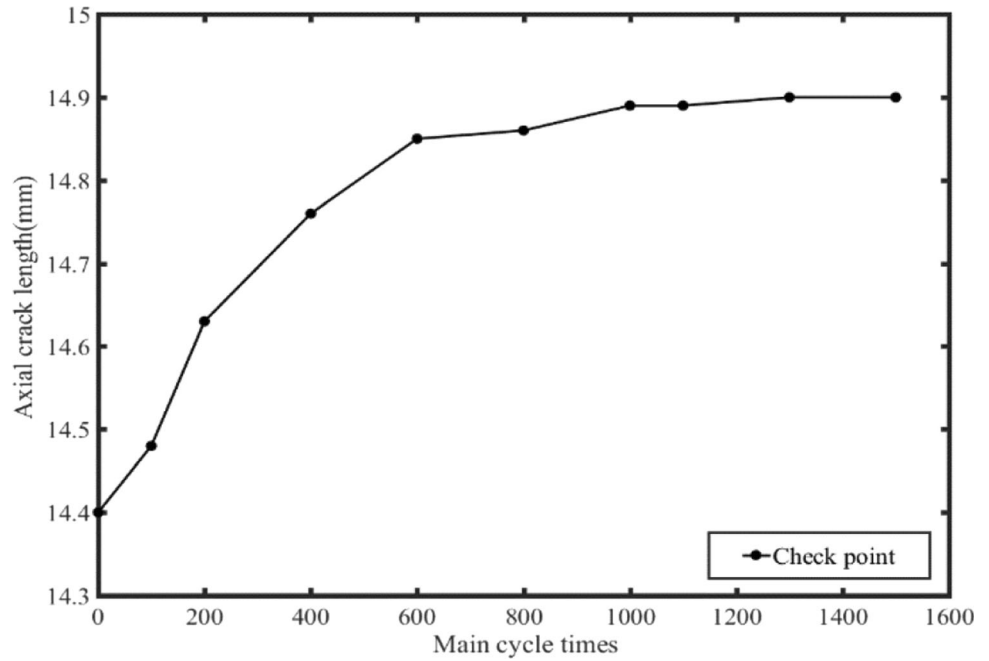
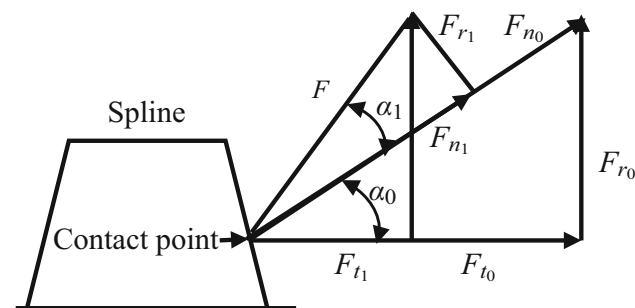
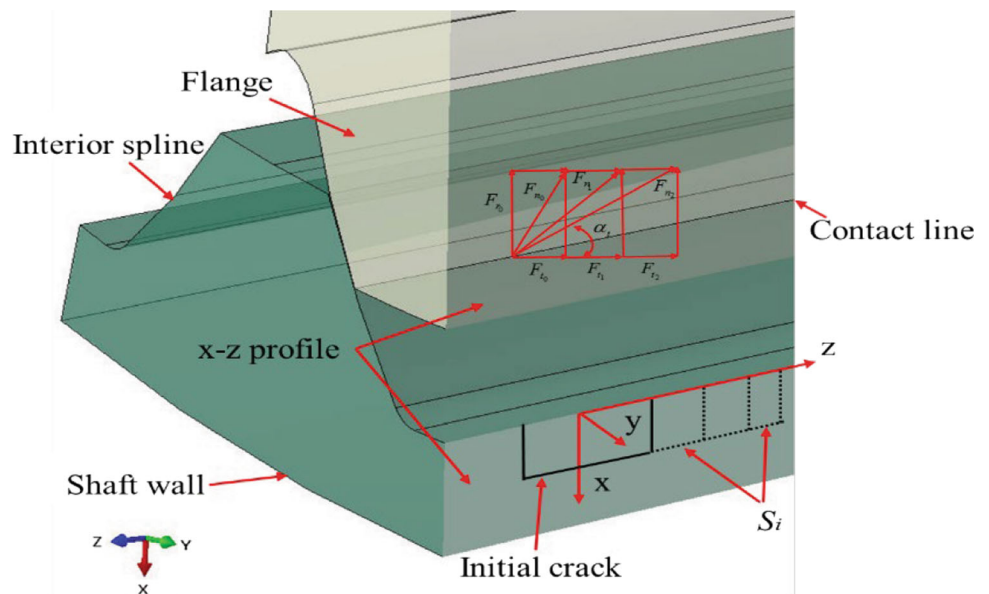


**Fig. 8** x-z section view of local contact



$$\Delta K_{eq} = \left( \frac{da}{CdN} \right)^{\frac{1}{m}} \tag{Eq 3}$$

Meanwhile,  $\Delta K_{eq}$  can write as [36]:

$$\Delta K_{eq} = \Delta K_I \cos^3 \frac{\theta}{2} - 3\Delta K_{II} \cos^2 \frac{\theta}{2} \sin \frac{\theta}{2} \tag{Eq 4}$$

where  $\Delta K_I = K_{I\max} - K_{I\min}$ ,  $\Delta K_{II} = K_{II\max} - K_{II\min}$ . The stresses of the crack tip are

**Fig. 9** Angle relationship of crack tip stresses

$$\begin{cases} \sigma_x = \frac{K_I}{\sqrt{\pi a_x}} \\ \sigma_y = \frac{K_{II}}{\sqrt{\pi a_y}} \end{cases} \quad (\text{Eq 5})$$

Combining Eqs. 1 to 5, the relation between  $\Delta K_{eq}$ , force components, and  $\alpha_i$  is:

$$\left(\frac{da}{CdN}\right)^{\frac{1}{m}} = \frac{T_M + T_S}{Tr} \cos^3 \frac{\theta}{2} - 3 \frac{T_M + T_S}{Tr} \tan \alpha_i \cos^2 \frac{\theta}{2} \sin \frac{\theta}{2} \quad (\text{Eq 6})$$

Due to the deformation of splines being tiny during the crack process, hence,  $\tan \alpha \approx \alpha$ . For convenience, the constants  $C_1$  and  $C_2$  are substituted for  $\left(\frac{da}{cdN}\right)^{\frac{1}{m}}$  and  $\frac{T_M+T_S}{Tr}$ , correspondingly:

$$C_1 = C_2 \cos^3 \frac{\theta}{2} - 3C_2 \alpha_i \cos^2 \frac{\theta}{2} \sin \frac{\theta}{2} \quad (\text{Eq 7})$$

By solving Eq. 7, the relationship of  $\alpha_i$  and  $\theta$  can write as:

$$\alpha_i = \left( \frac{1 + \cos \theta}{3 \sin \theta} - \frac{2C_1}{3C_2 \cos^2 \frac{\theta}{2} \sin \theta} \right) \quad (\text{Eq 8})$$

Based on Eq. 8, the force components of cracked components can be calculated as follows:

$$\begin{cases} F_{ti} = C_1 \frac{1}{\sqrt{\pi a}} \\ F = \frac{F_{ti}}{\cos \alpha_i} \\ F_{ni} = F * \cos(\alpha_i - \alpha_0) \end{cases} \quad (\text{Eq 9})$$

Then, the contact stress between splines can be solved by introducing the new normal force  $F_{ni}$ , and tangential force  $F_{ti}$  into the Hertz model and AGMA standard.

Contact Stress of 14.4–14.9 mm Growth Stage

Due to the radial crack length in the surface not changing in the 14.4–14.9 mm growth stages, this means the radial force on the loaded side is not large enough to provide the required force for growth in the crack front. Hence,  $K_{II}$  can be excluded in Eqs. 4 and 5, the angle between the force component is:

$$\alpha_i = \arctan \frac{C_2 - C_1}{3C_2} \quad (\text{Eq 10})$$

And the  $\sigma_x$  in the crack front is:

$$\sigma_x = C_1 \frac{1}{\sqrt{\pi a}} \quad (\text{Eq 11})$$

From this, the normal force is  $F_{ni} = \sigma_x * \cos(\alpha_i - \alpha_0)$  and the contact stress is determined in the same way as in the 0–14.4 mm growth stages.

Crack Growth

Cracks [37, 38] can be classified into three patterns according to their surface displacement types as shown in Fig. 10. In practice, either the single or combination crack pattern may appear due to the different loads. Figure 11 gives an overview of the progressive process to estimate the path of FCG with finite element software. When the crack appears, the global or the local geometry will change, so the meshing of the finite model should be updated. However, because the crack is tiny and just a local area in the whole model, the partial region around the crack should be re-meshed. We use ABAQUS (or ANSYS) to complete the preprocessing and solving, then input the post-process file into the FRANC3D to make crack growth. Finally, the crack growth results will be reintroduced into ABAQUS (or ANSYS) to analyze the contact stress.

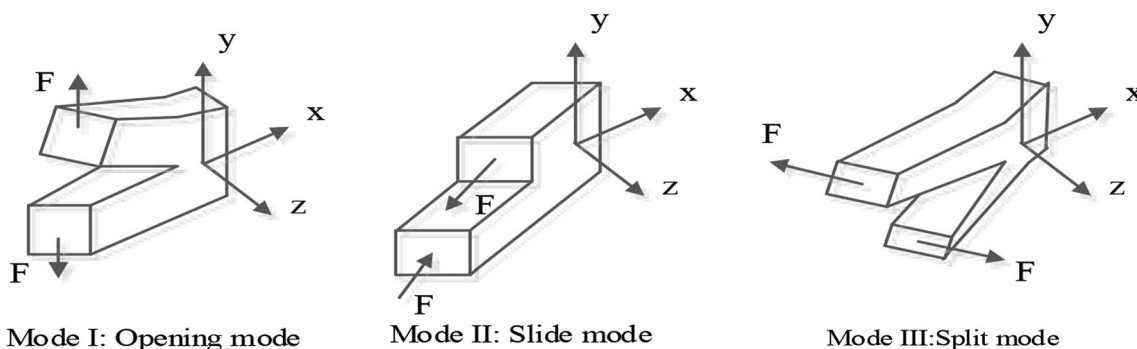
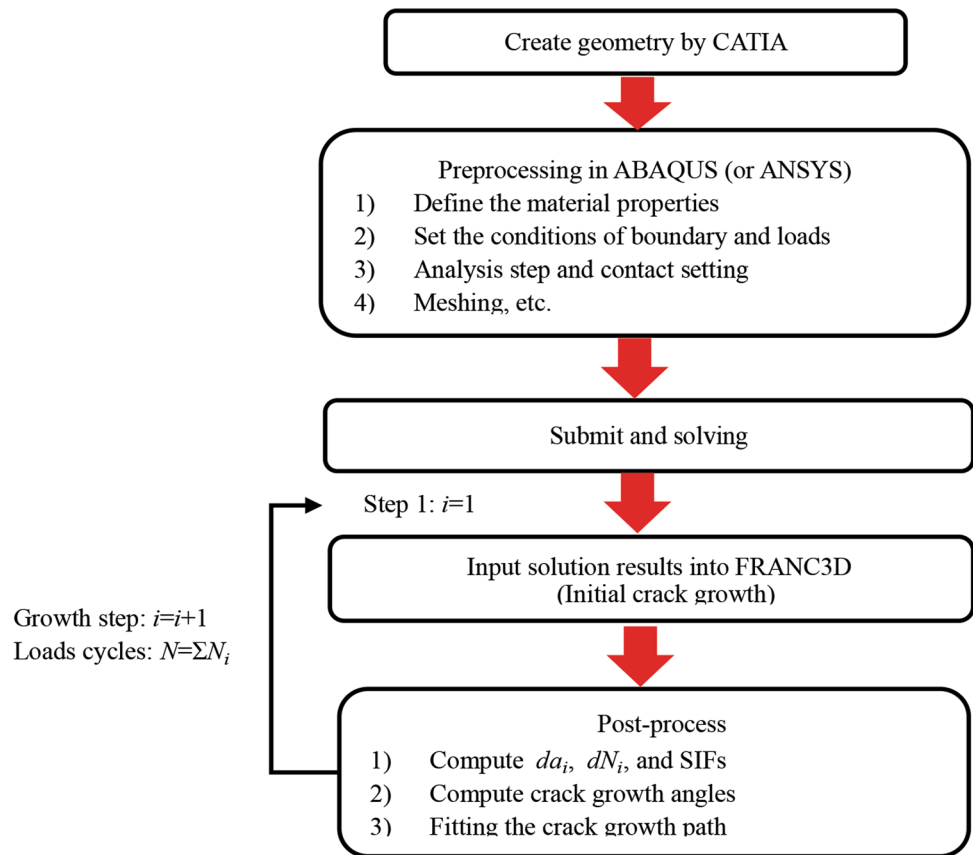


Fig. 10 Schematic diagram of crack modes

**Fig. 11** Flow diagram of crack growth path prediction



In each growth stage, the FCG ratio and growth angle can be calculated at each integral point by the corresponding SIFs. According to the maximum circumference principle and modified Paris model [36], the crack growth angle  $\theta$  is:

$$\sigma_{\theta} = \frac{\cos \frac{\theta}{2}}{2(2\pi r)^{1/2}} [K_I(1 + \cos \theta) - 3K \sin \theta] \quad (\text{Eq 12})$$

Making the  $\sigma_{\theta}$  becomes max. That is:  
 $\partial \sigma_{\theta}(K_I, K_{II}) / \partial \theta = 0$ :

$$K_I \sin \theta + K_{II}(3 \cos \theta - 1) = 0 \quad (\text{Eq 13})$$

And

$$\theta = \arccos \frac{3K_{II}^2 \pm \sqrt{K_I^4 + 8K_I^2 K_{II}^2}}{K_I^2 + 9K_{II}^2} \quad (\text{Eq 14})$$

Then, the offset angle of contact stress can be determined by substituting Eq. 14 into Eq. 8.

#### Stress Intensity Factors History

The former analysis illustrates that SIFs play a prominent role in the path prediction of the FCG. Hence, it is

necessary to understand the property and change tendency of SIFs before predicting the crack growth path.

Figure 12a plots the SIFs variation over a growth process for a point of the crack front. The value of SIFs is presented as functions as the crack length (or crack growth stage). Due to the SIFs reflecting the stress field strength of the crack front, therefore, this trend reminds us the stresses in the crack front are non-proportional and will lead to different crack growth ratios in the radial and tangential.

Figure 12b illustrates that the complicated loads will produce a non-proportional stress field on the contact region when the crack appears. Accordingly, the maximum circumference stress laws can be utilized to calculate crack growth angles for each growth stage. What is wanted, whereas is the crack growth path at the end of each growth stage. The most mentioned papers in the introduction focus on experiments or artificial cracks and only a few kinds of literature deal with crack growth path prediction [21–23, 26]. At the same time, the majority of work is limited to the two dimensions analysis [30–33, 35]. Given the mentioned drawbacks, a method is proposed and applied to make FCG path predictions for the transmission shaft.



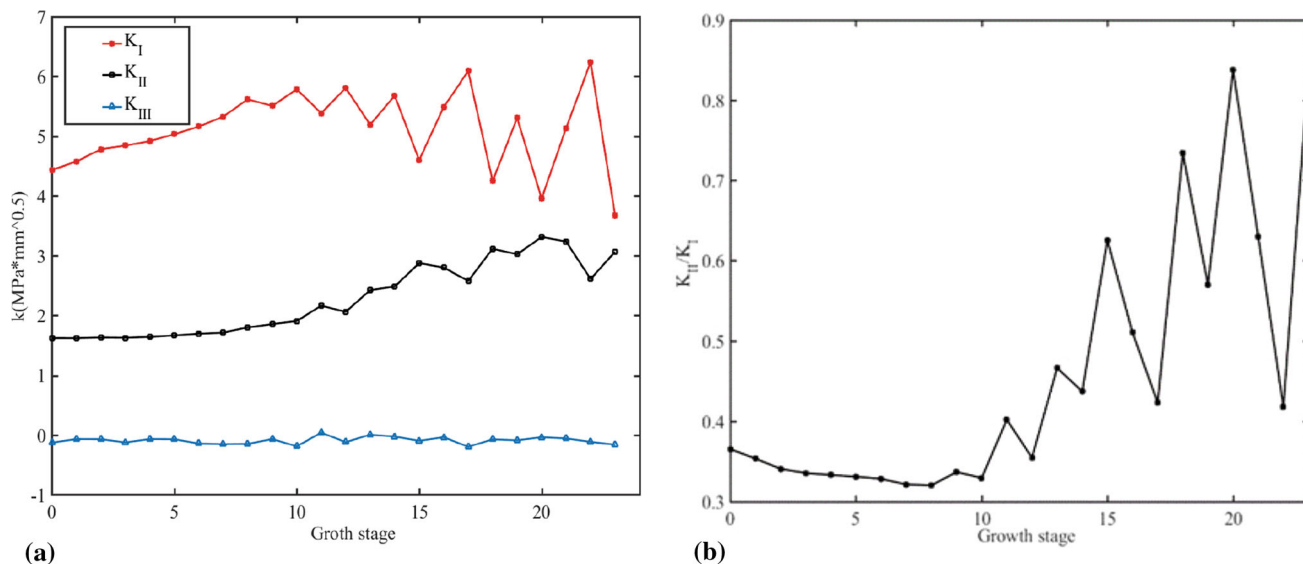
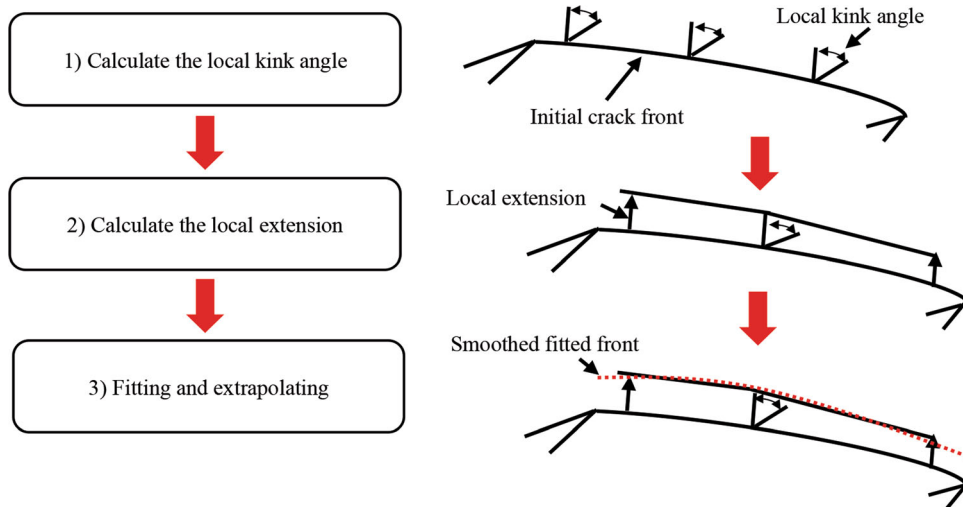


**Fig. 12** SIFs history (a) and loads cycle (b) at the fixed point of the crack front

**Fig. 13** Steps of path prediction of FCG



*The Path Prediction of FCG with Periodic Load*

Figure 13 summarizes the path prediction of FCG with periodic load in three steps after the property of SIFs are determined, and the specific procedures are given as follows.

This paper divides the continuous crack growth in cycle times into a succession of growth stages, or contact stress levels, as described in “Contact Stress” Section. Based on the two-dimensional crack growth theories, reference [20] summarized a method to predict FCG path in three dimensions that SIFs change with loading cyclic count. However, some necessary modifications are done to make it holds in this paper.

- (1) Separate the continuous crack growth process into discrete stages according to the crack length.

- (2) Calculate the SIFs ( $K_{Ij}^i, K_{IIj}^i, K_{IIIj}^i$ ) in every growth stage. Here,  $i$  ( $i = 1 \sim$  last point) is the discrete point around the crack front,  $j$  ( $j = 1 \sim 24$ ) represents the growth stages.
- (3) Calculate crack increment  $da_{(j-1,j)}^i$  of every given point of two successive growth stages  $j$  and  $j + 1$ .  $\theta_{(j-1,j)}^i$  is the extension of the crack growth angle from stage  $j$  to  $j + 1$ . Besides, it is suggested that the increment of the crack growth process always keeps positive,  $K_{Ij}^i - K_{I,j-1}^i > 0$ .

To improve the precision of the analysis of crack growth over each stage, this paper considers the equivalent SIFs. The count of extension in each stage,  $da_{(j-1,j)}^i$ , can be calculated through Eq. 3. In addition, it is supposed that the

crack length increment of two growth stages is proportional to the ratio of SIFs:

$$\frac{da_{(j-1,j)}^i}{da^i} = \frac{K_{Ij}^i - K_{I(j-1)}^i}{\Delta K_{eq}} \tag{Eq 15}$$

At the same time, the crack growth angle can be calculated by Eq. 14.

- (4) Get the last coordinates and path angle of a specific point in every growth stage by repeating step (3), then, connect the final coordinates of all the given points from the crack tip to the last crack growth position. This step can be illustrated in Fig. 14 if the process includes four crack growth stages.

Since the crack growth is a tiny and gradual process, it can be assumed that dash straight line is approximate to replace the arch curve, which is the sum length of crack extension  $da_{(j-1,j)}^i$ . Then the crack growth angles  $\theta_j^i$  can be attained by analyzing the last point coordinates.

- (5) Complete steps (3) and (4) for every point in the circumferential area of the crack front.
- (6) Calculate the loading cyclic times,  $N$ , and the count of crack growth is dependent on shaft geometry. This is a key procedure due to the crack growth is too small to refresh the simulated model in one growth stage. Hence, it is assumed that continuous crack growth has taken place before the geometry model changes. Because every point around the crack front has a particular growth ratio and kink angle, the crack front in every stage is not grow consistently. The last growth amount ( $da_{last}^i$ ) of every point is

$$da_{last}^i = Nda_T^i \approx \sum_{i=1}^n da_{(j-1,j)}^i \tag{Eq 16}$$

- (7) Renew the finite element model after the new crack is grown with a count  $da_{last}^i$ . The ultimate crack growth path can be fitted by regression analysis. When the crack model is refreshed, submit the re-meshing model to the finite element software, and repeat this stage until all the growth stages are analyzed with the new crack.
- (8) Repeat the analysis process and start from the procedure (2) for a new growth stage.

### Simulation of Contact Stress and Crack Growth Path

#### Finite Element Model

The global and local finite element model of the transmission shaft are shown in Fig. 15. According to boundary and loading conditions, the flange contacts with the interior splines is fixed, and torque is loaded on the flange that assembles with the exterior splines. Due to all the components belonging to the central symmetry structure, 1/12 of the assembly can be selected as the local model to insert the initial crack. Besides, to ensure the accuracy of the simulation, the meshing amount and quality in the contact regions, edges, and fillets are refined.

#### Simulation of Contact Stress

For simulating the contact stress between the splines of each growth stage. This paper separates the whole crack growth process into two stages: the crack initiation stage

**Fig. 14** Illustration of specific point extension of crack front in a crack growth process

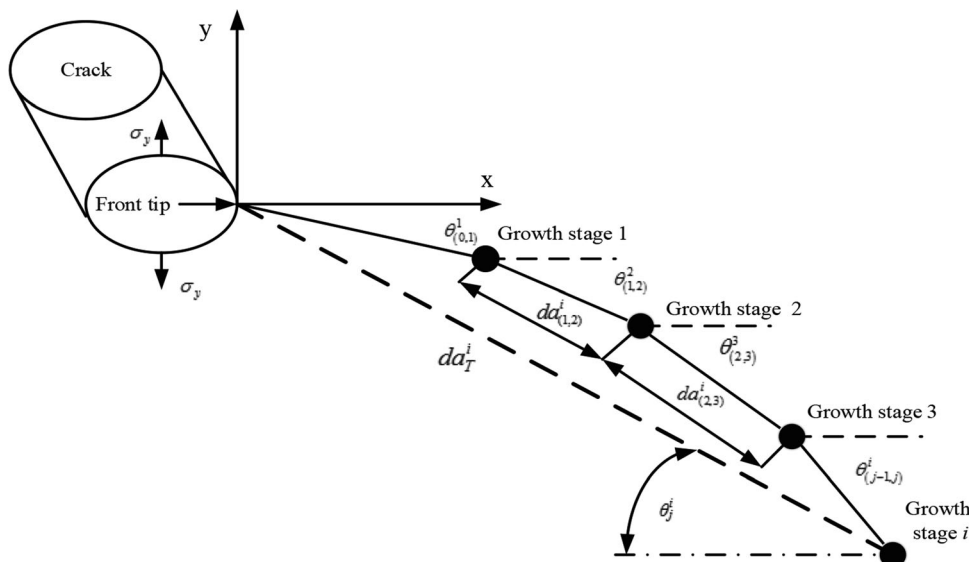
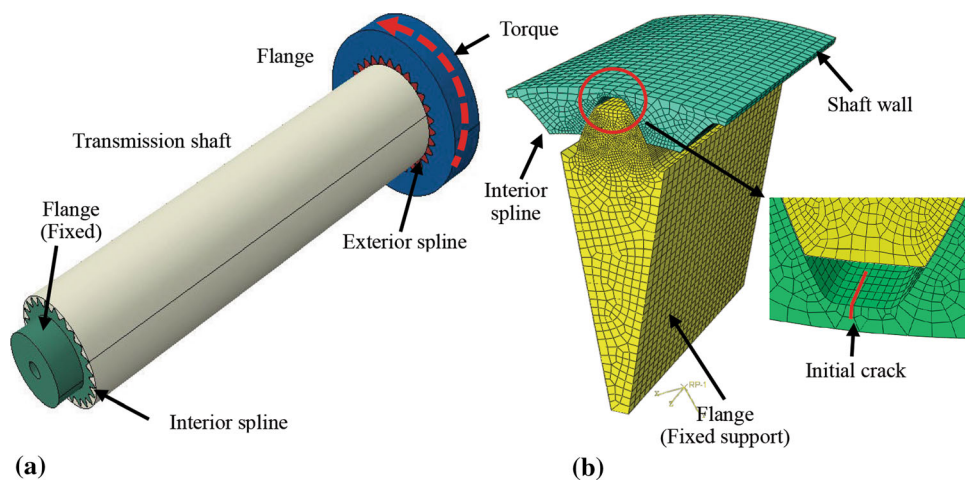


**Fig. 15** Global (a) and local (b) finite element model of transmission shaft with initial crack ( $N = 0$ )



and the FCG test stage. Every analysis stands for one of the 24 crack growth stages when the contact stress change with the crack length.

Table 1 presents the contact stress for the local model with and without cracks by the simulation and theoretical method. The statistical data unfold that: (1) Contact stresses between the splines show a downtrend in the whole growth process either for the simulation or the theoretical calculation; (2) Contact stress appears to level off and almost remain constant when the crack length approaches the failure threshold.

The comparison results illustrate contact stress can be treated as a failure criterion when a cracked component works with complicated loads. Meanwhile, the fracture mechanic parameters and crack growth path can be researched based on the contact stress analysis.

**Results**

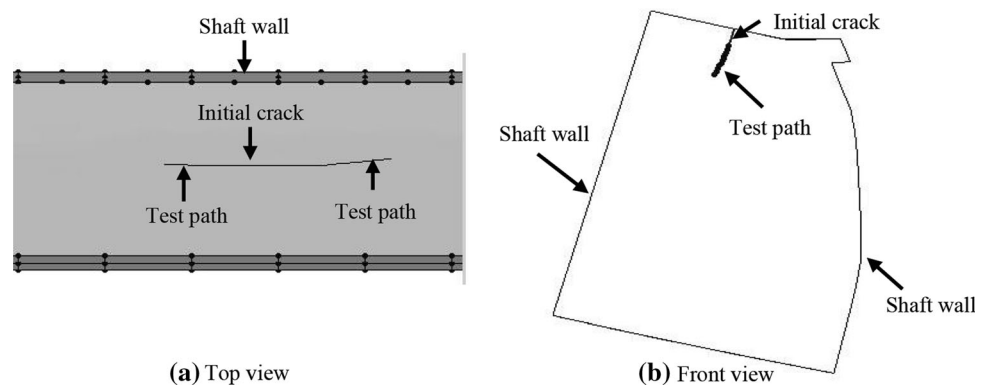
Periodic Load Method

Figure 16 is the predicted crack growth path along the axial (top view) and the radial (front view) by the method described in “Crack Growth” section. The section view is chosen near the location along the tooth width of the fixed point of the initial crack front. The crack growth path is measured and observed by magnetic testing after the FCG experiment. The initial crack is introduced into the finite element model and then simulated according to the test set. Therefore, it is found that the simulation does not thoroughly fit the test situation and the additional growth of crack may not lead to a better perception. Hence, the crack growth path does not show a straight line on the surface of the shaft wall and kinks toward to shaft wall in the section view. A possible reason for the difference between the simulation and the experiment because the simulation did

**Table 1** Contact stress comparison between theoretical method and simulation

		Contact stress without crack (MPa)			
		Hertz theory	AGMA standard	Simulation	
		195.47	195.97	ABAQUS 195.60	ANSYS 194.23
		Contact stress considering crack (MPa)			
Stages of initial crack growth	Crack length (mm) $a_x/a_y$	Hertz theory	AGMA standard	Simulation	
		(Modified)	(Modified)	ABAQUS	ANSYS
1	0.68/0.1	190.53	192.76	193.15	192.86
2	0.72/0.1	185.11	183.12	192.23	192.39
3	0.75/0.1	185.01	183.15	191.55	192.28
4	0.81/0.12	185.03	183.13	190.90	192.20
5	0.97/0.14	185.01	183.111	190.66	191.83
6	1.17/0.17	185.00	183.14	190.02	191.11
7	1.4/0.21	185.02	183.06	188.92	190.49
8	1.68/0.25	184.96	184.36	188.04	189.70
9	2.02/0.3	185.05	184.17	187.79	188.58
10	2.42/0.38	184.96	183.05	187.18	187.89
11	2.90/0.43	184.39	182.37	186.31	187.66
12	3.48/0.52	184.11	182.07	185.43	186.44
13	4.18/0.62	183.56	181.46	184.57	185.12
14	5.02/0.74	183.28	181.23	183.70	184.77
15	6.02/0.89	182.87	180.89	182.83	177.92
<i>Stages of FCG test</i>					
16	7.2/1	181.97	180.03	179.92	180.36
17	7.24/1	181.06	179.22	179.01	178.67
18	7.315/1	180.52	178.87	178.65	179.59
19	7.38/1	180.16	178.77	178.58	178.74
20	7.425/1	179.54	178.50	178.51	179.44
21	7.43/1	178.37	178.68	179.29	179.73
22	7.445/1	178.48	177.93	178.72	179.74
23	7.45/1	179.08	178.96	179.21	179.55
24	7.5/1	179.02	178.88	178.14	179.77

**Fig. 16** Predicted crack growth path compared with the test results ( $N = 4e6$ )



not consider the size change of geometry when the crack grows. Besides, the loading location is another reason that can influence the crack growth path in the experiment, the size and location of the contact region in each stage were regarded as constant during the simulation. However, in practice, the elastoplasticity deformation of the spline can trigger the contact location and stress distribution change to the next stages while the system running. The effect of load location on the crack growth path is going to be discussed in chapter 6.

A further detailed comparison between the simulation and theoretical analysis is made. The theoretical analysis of spline failure is consistent with the FCG test. In addition, no matter the simulation and test, the crack growth ratio in the early stages is faster than in the later stages. However, some splines' roots and surfaces keep intact on both sides. The simulation shows the crack growth has an obvious kink tendency toward the root of the spline no matter in the surface or the interior. This situation was confirmed in the test.

The crack growth path predicted in the depth of the shaft wall after  $4e6$  cycles are almost in accord with the practical crack path. It is concluded that the crack growth will cause deformation or fracture of the spline if the simulations are sustained. The final crack growth path, whereas does not entirely fit the FCG test. Compared with the FCG test, the simulated crack path shows a tendency to approach the spline root. A possible explanation for this difference may be the transmission shaft was tested under a complicated load, whereas the simulation was for constant loads and did not consider the dynamic impact and fluctuation of the applied torque. The variable torque magnitude, indeed, will affect the contact stress, and conversely, will influence the crack growth path. The sensitivity of the crack path to torque level and loading position will be studied in “Discussion” section.

During the FCG, the crack length in axial and radial are measured every 200 (or 100) main cyclic times. Hence, the fatigue life data accessible from the test is an upper limit of the main cycle times (or the crack length). Figure 17 is a

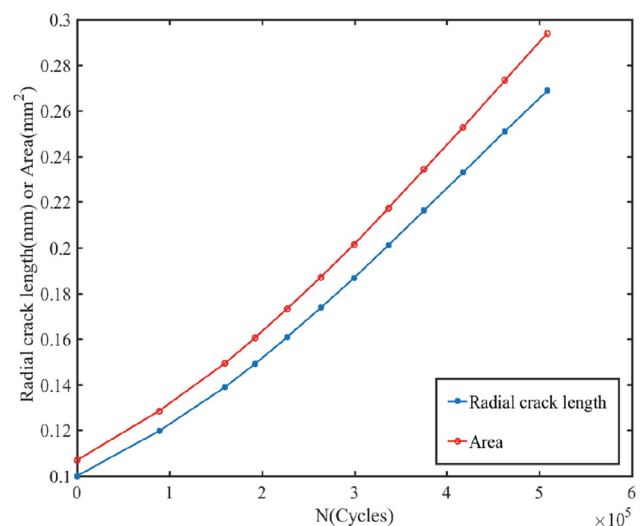


**Fig. 17** Predicted crack length and crack area versus a count of cycles

diagram of the simulation fatigue life for the cyclic loading method. The position in the tooth thickness direction of the center point is set as the reference to measure the crack size, which is plotted corresponding to the count of loading cycles. Meanwhile, the crack area is also plotted as the function of the loading cycle times for comparison when the crack depth change with the crack length.

Considering the SIFs from the growth stage 16 and the axial growth ratio, it is estimated that more than 2300 additional main cycles were needed when the crack front grows to the  $2/3$  spline width.

#### Alternative Load Method

To assess the other specifics of the cyclic loading method, another prediction is explored that set the loading process as Fig. 18 shows. The alternative load chooses stage 16 as the initiation of load since it is the first stage that the crack length of the radial keeps stable but still increases in the axial. An applied torque ( $T = 3552.5 \sin(2t) \text{ N}\cdot\text{mm}$ ) is

loaded on the contact region. Other parameters, such as material property, initial crack length, and model size are the same as the periodic load method. In addition, the direction of crack growth was also determined by the maximum extension stress principle through the ratio of SIFs, and the increment of crack growth and cyclic times can be calculated by Eq. 2.

Figure 19 gives the crack growth path of the alternative load method after about  $4e6$  cycles. Compared with the periodic load method, the simulated path of alternative load performed an obvious kink angle on both ends of the shaft wall surface; Secondly, the crack growth path of the alternative load method produce a steeper kink angle in the interior view.

On the surface of the shaft wall, the crack growth path fits better with the test in the initial growth stages. But the crack path in the interior does not match the test well. In the front view of the section, the alternative load causes a

larger kink angle than the periodic loading. The final purpose of the simulation is to recognize the failure of the transmission shaft since a precise crack growth path on the surface and in the interior view is prominent. Given this, the periodic load can attain a better simulation in three dimensions.

### Discussion

In this section, research is presented to achieve an understanding of the influence of the loading location and magnitude to predict growth path and growth ratio. The research is also intended to study the feasible inducements of the difference between simulation and experiment. The discord between the periodic load prediction and test is mainly due to the inaccurate description in the simulation of the practical contact region in the experiment. The residual parts of this section are to study whether the changed loads with different crack locations have identical affection to the crack growth path.

#### Changed the Loading Location

Two loading locations are researched. For both situations, the finite element model from the growth stage 16 is simulated with the shifted contact region. This stage is chosen due to it is the first stage of the FCG experiment. The contact regions will offset  $\pm 0.2$  mm from the pitching circular along the spline height.

The crack growth path with different contact regions is simulated by the method described in “[Analysis of Contact Stress and Crack Growth Path](#)” section. Table 2 plots the simulated path on the surface of the shaft wall with the initial crack and two shifted locations analysis.

When the loading location was at the pitch circle, the crack path on the surface of the shaft wall almost keep in straight along the axial on both ends. But, when the loading

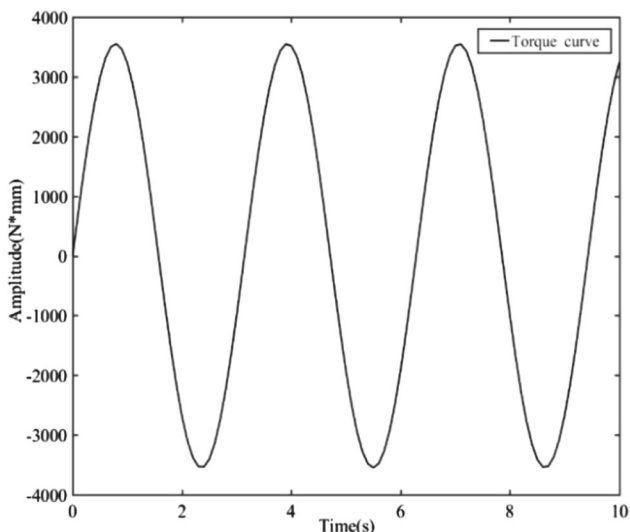
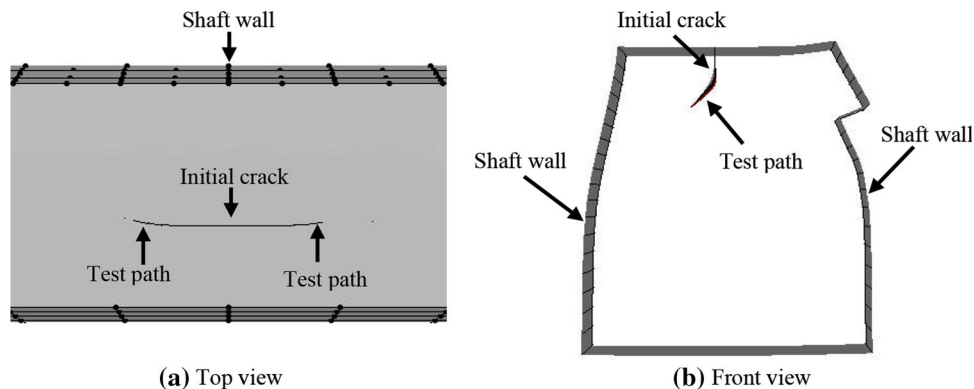
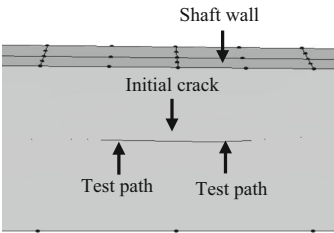
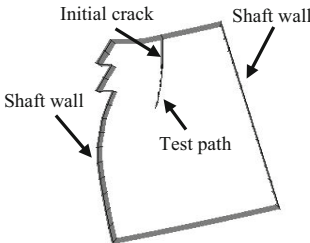
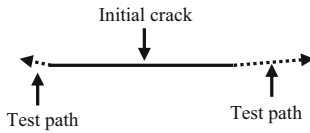
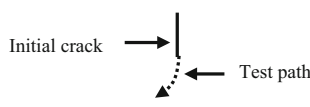
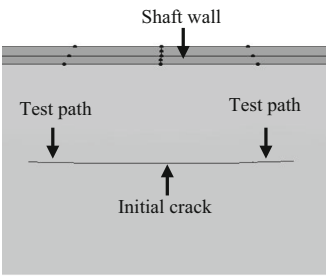
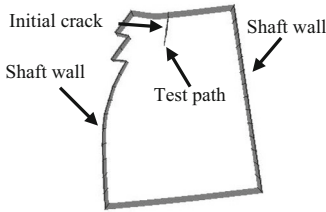
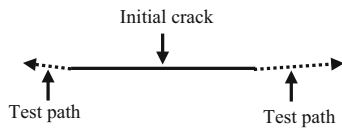
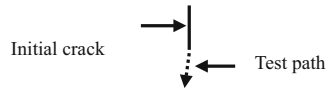


Fig. 18 Torque loading curve

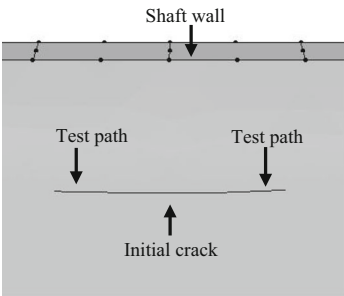
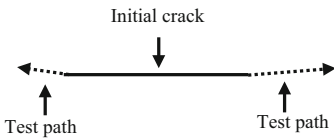
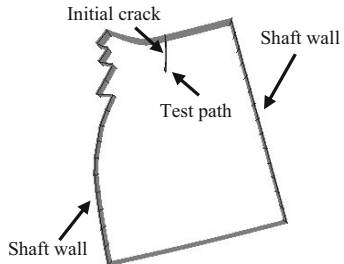
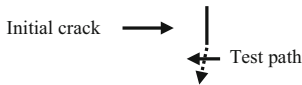
Fig. 19 Crack growth path with alternative load



**Table 2** Crack growth path comparison shifted along the tooth height

Loading location	Crack growth path on the surface and interior
<p>1. Shifted up 0.2 mm</p> <p>Surface (Top view)</p>  <p>Interior (Front view)</p> 	 
<p>2. Pitch circle</p> <p>Surface (Top view)</p>  <p>Interior (Front view)</p> 	 

**Table 2** continued

Loading location	Crack growth path on the surface and interior
<p>3. Shifted down 0.2 mm</p> <p>Surface (Top view)</p> 	
<p>Interior (Front view)</p> 	

**Table 3** Parameters of AGMA standard

Parameters	Physical meaning	Remarks
$C_p$	Elastic constant factor	See Eq. 19
$F_t$	Transverse force	
$b$	Contact line length	Straight gear
$d$	Pitch circle radius	
$I$	Geometry factor	See Eq. 20
$\beta$	Helix angle	0°
$CR$	Contact ratio	See Eq. 21
$K_u$	Velocity factor	See Eq. 22
$K_v$	Overload factor	Mechanical design handbook
$K_m$	Load distribution factor	Mechanical design handbook

position shifted up, the growing tendency toward the left side of the shaft wall is restrained gradually and slower than the growth ratio of the right side. When the loading location moves down, the torsion tendency of both ends becomes more apparent (Table 3).

On the other side, the crack growth in the interior also shows a different path. Specifically, the crack growth keep

nearly straight when the loading location was at the pitch circle and shifted down. However, the crack shows a clear kink tendency when the loading shifted up. These results verified the assumption in reference [39] that different loading distributions along the tooth width have a significant influence the crack growth.

The difference in the crack growth path in the surface and interior between the simulation and experiment can be explained by the truth that, in the experiment, the crack can cause tiny deformation in the local geometry, and the contact region gradually moves away from the root of the spline. Meanwhile, the loading distribution along the spline height has been changed due to the reduced stiffness of the structure. A slight change in the load distribution or their impacts on the crack path can be predicted by a three-dimensional analysis of meshing gears with a finite element simulation. At present, there have been studies on the change of contact stress with crack growth.

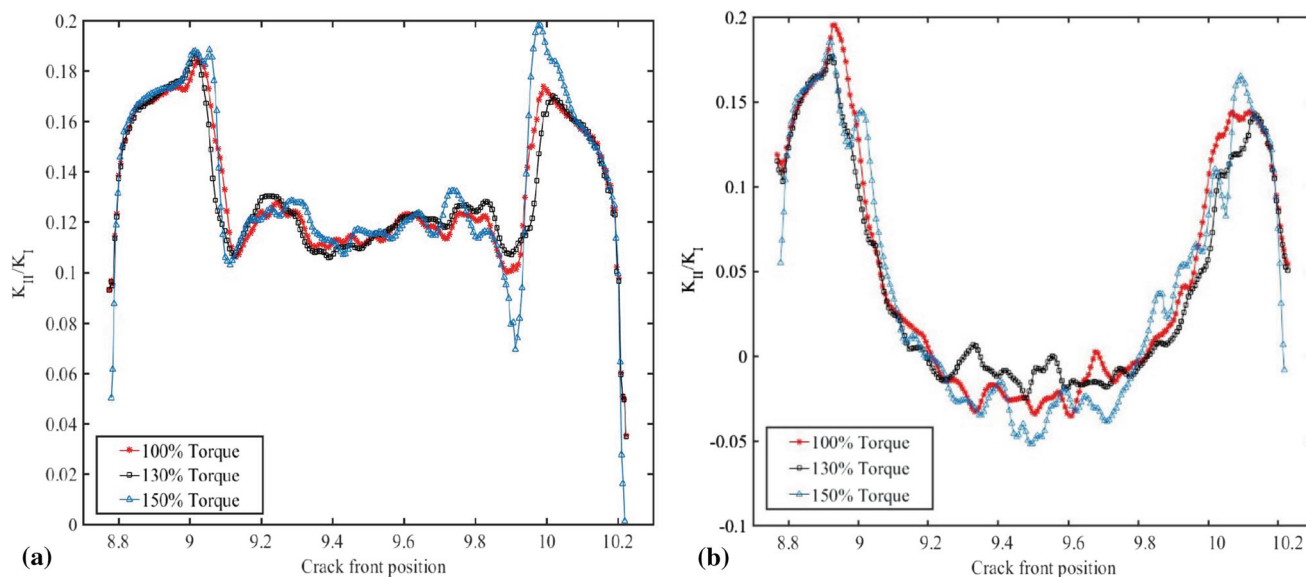


**Fig. 20** Distribution of  $K_{II}/K_I$  in crack growth stage 16 (a) and stage 20 (b)

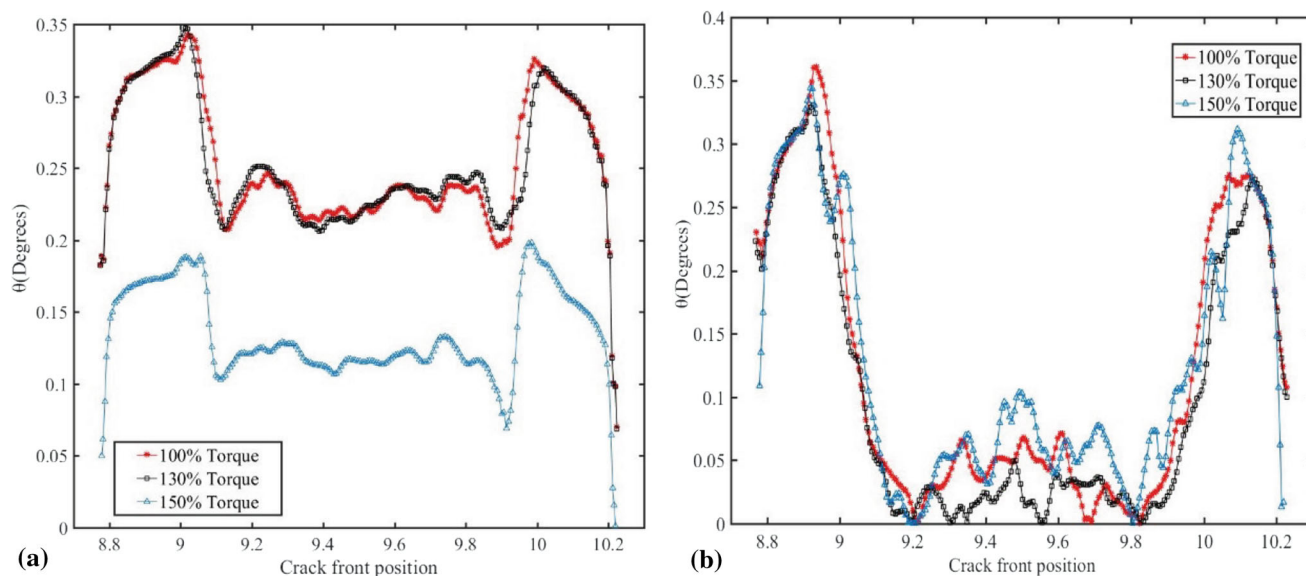


**Fig. 21** Crack growth angle variation for growth stage 16 (a) and growth stage 20 (b)

### Changing Load

The input torque of the FCG experiment varied from 77.51 to 85.26 N\*m. However, in practice, overload is a common situation for transmission shaft. The purpose of the present research is to find out the influence of the increased torque on the crack growth path.

Here, the simulation chooses the torque magnitude of 110.84 N\*m and 127.89 N\*m (130% and 150% maximum torque) to explore the change rule of SIFs and crack growth path. According to the Hertz theory, the maximum contact

stress is proportional to the square root of the normal force. Accordingly, if the applied load increases, the contact stress will change simultaneously. Similar to the shifted loads research, the growth stage 16 in the periodic load simulation is chosen to investigate the new torque levels.

During the simulation and theoretical calculation, the ratio of  $K_{II}/K_I$  is a key index because it determines the crack growth angle and the contact stress between the splines. A higher ratio means a larger crack growth angle. In addition, due to the SIFs representing the stress strength of the crack tip, an incremental ratio can cause contact



stress to rise between the splines. The ratios of  $K_{II}/K_I$  of growth stage 16 and stage 20 are plotted in Fig. 20. These curves illustrate that the ratio of  $K_{II}/K_I$  increased as the stress and location of contact region changed. This result supposed that  $K_I$  is more sensitive to the change of the torque magnitude than  $K_{II}$ . This fact demonstrates by magnetic testing, that is, the mode I crack plays a major role during the entire FCG.

The percentage of fracture splines is an important signal of contact stress of the assembly. In the initial crack growth stage, the SIFs ratio may not be large enough to verify the level change of stress observed. Otherwise, it seems that a rising torque magnitude can be used to explain the stress level between the contact splines.

The crack growth angles can be calculated by the methods in “Crack Growth” section for three torque magnitudes and two locations shown in Fig. 21. The crack growth angles vary range from 0 to  $0.4^\circ$ . These curves give evidence of how the torque levels can influence the crack growth path.

### Conclusions

This work made a deep investigation of the contact stress and the FCG path for the cracked transmission shaft. To attain accurate analysis and simulations, it needs to extend the latest methods to predict the path and ratio of crack growth. This research concerns the contact stress change with crack growth by improved Hertz theory and AGMA standard, equivalent SIFs, and crack growth path with three dimensions. The local finite element model is utilized to simulate the crack growth path combined with the fracture mechanics theory. Moreover, the influence of loading positions and strength are explored on the crack

growth path and fatigue life analysis. Some key issues have been verified as vital to attain accurate simulations as follows:

1. Making the contact stress analysis of cracked structure is an efficient way to avoid fracture failure occurring, meanwhile, it reflects the state of the running system.
2. Compare with the two-dimensional analysis for the FCG path, setting a three-dimensional local finite element model is necessary for the complex geometry model.
3. The different loading locations and magnitudes between the splines have a significant impact on the kink and development tendency of crack growth
4. Modeling for the different stages in a continuous crack growth process is critical before the three-dimensional results need to be performed.

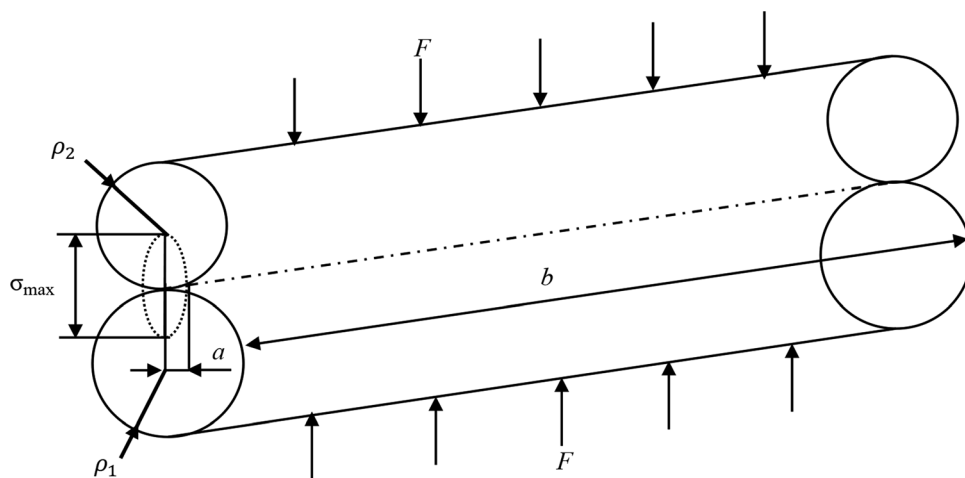
**Acknowledgments** This project is supported by the National Natural Science Foundation of China (Grant No. 52075443). Basic Research Program of Natural Science of Shaanxi Province of China (No.2020JM-113).

### Appendix

#### Hertz Theory

Hertz theory is based on the elastic mechanic, which can be used to describe the local stress of contact objects, it has three assumptions:(a) The contact objects are linear elastic bodies; (b)The contact area is smooth; (c)The size of the contact area is an infinitesimal variable compared with the cylinder curvature radius. This contact relation can illustrate in Fig. 22.

**Fig. 22** Schematic diagram of Hertz contact model



The contact stress (elliptic in dash area) of two cylinders is:

$$\sigma_{\max} = \sqrt{\frac{F_s}{\pi b} \left( \frac{\frac{1}{\rho_1} + \frac{1}{\rho_2}}{\frac{1-\mu_1^2}{E_1} + \frac{1-\mu_2^2}{E_2}} \right)} \quad (\text{Eq 17})$$

where  $F_s$  is the normal stress of contact faces,  $b$  stands for the length of the contact line,  $\rho_i$  ( $i = 1, 2$ ),  $\mu$ , and  $E$  represents the curvature radius, Poisson ratio, and elastic modulus of contact objects.

### AGMA Standard

The definition and parameters of the AGMA standard are presented as follows [40]:

$$\sigma_{\max} = C_p \sqrt{\frac{F_t}{bdI} \left( \frac{\cos \beta}{0.95CR} \right) K_u K_v (0.93K_m)} \quad (\text{Eq 18})$$

$$C_p = 0.564 \sqrt{\frac{1}{(1-\mu_1^2)/E_1 + (1-\mu_2^2)/E_2}} \quad (\text{Eq 19})$$

where  $E$  and  $\mu$  stand for Young's modulus and Poisson ratio.

$$I = \frac{\sin \alpha \cos \alpha}{2} \frac{i}{i+1} \quad (\text{Eq 20})$$

where  $i = \frac{d_2}{d_1}$  is the speed ratio,  $\alpha$  is the transverse pressure angle.

$$CR = \frac{\sqrt{(R_1 + a)^2 - R_{b1}^2} + \sqrt{(R_2 + a)^2 - R_{b2}^2} - (R_1 + R_2) \sin \alpha}{\pi m \cos \alpha} \quad (\text{Eq 21})$$

where  $R$ ,  $R_b$ , and  $a$  represent the pitch circle radius, base circle radius, and addendum, respectively. Suffix 1 is for the interior spline and 2 is for the flange,  $m$  is the modulus that equals 2.5 mm.

$$K_u = \left[ \frac{78 + (200V)^{\frac{1}{2}}}{78} \right]^{\frac{1}{2}} \quad (\text{Eq 22})$$

$V$  is rotation velocity or pitch line velocity.

### References

1. J.S. Millan, I. Armendariz, J.G. Martinez, R. Gonzalez, Strategies for static failure analysis on aerospace structures. ISBN: 9780128009505. Chapter 1, pp. 20–26. Chapter 2, pp. 34–43, Chapter 5, pp. 88–98
2. Y. Feng, F.Z. Yuan, T.Z. Dan, Simulation analysis of gear contact stress in reduction gearbox. *J. Phys. Conf. Ser.* **1748**, 062072 (2021). <https://doi.org/10.1088/1742-6596/1748/6/062072>
3. Y.S. Zhai, J. Mu, R.G. Yun et al., Analysis of tooth surface contact stress of involute spur gear. *J. Phys. Conf. Ser.* **2133**, 012037 (2021). <https://doi.org/10.1088/1742-6596/2133/1/012037>
4. S.H. Wu, S.J. Tsai, Contact stress analysis of skew conical involute gear drives in approximate line contact. *Mech. Mach. Theory.* **44**, 1658–1676 (2009). <https://doi.org/10.1016/j.mechmachtheory.2009.01.010>
5. G. Vukelic, D. Pastorcic, G. Vizin, Failure analysis of a crane gear shaft. *Proc. Struct. Integr.* **18**, 406–412 (2019)
6. V.I. Medvedev, A.E. Volkov, M.A. Volosova et al., Mathematical model and algorithm for contact stress analysis of gears with multi-pair contact. *Mech. Mach. Theory.* **86**, 156–171 (2015). <https://doi.org/10.1016/j.mechmachtheory.2014.12.005>
7. I.G. Perez, J.L. Iserte, A. Fuentes, Implementation of Hertz theory and validation of a finite element model for stress analysis of gear drives with localized bearing contact. *Mech. Mach. Theory.* **46**, 765–783 (2011). <https://doi.org/10.1016/j.mechmachtheory.2011.01.014>
8. W.J. Qin, C.Y. Guan, An investigation of contact stresses and crack initiation in spur gears based on finite element dynamics analysis. *Int. J. Mech. Sci.* **83**, 96–103 (2014). <https://doi.org/10.1016/j.ijmecsci.2014.03.035>
9. Y.G. Wei, X.J. Zhang, Y.K. Liu, Theoretical research on the maximum contact stress of involute spur cylindrical gear pairs in the external meshing process, in *2010 International Conference on Mechanic Automation and Control Engineering*. 26–28 June 2010, (Wuhan). Pp. 491–495. <https://doi.org/10.1109/MACE.2010.5536561>
10. S.S. Patil, S. Karuppanan, I. Atanasovska, A.A. Wahab, Contact stress analysis of helical gear pairs, including frictional coefficients. *Int. J. Mech. Sci.* **85**, 205–211 (2014). <https://doi.org/10.1016/j.ijmecsci.2014.05.013>
11. S.C. Hwang, J.H. Lee, D.H. Lee, S.H. Han, K.H. Lee, Contact stress analysis for a pair of mating gears. *Math. Comput. Model.* **57**, 40–49 (2013). <https://doi.org/10.1016/j.mcm.2011.06.055>
12. G. Vukelic, D. Pastorcic, G. Vizin, Z. Bozic, Failure Investigation of a Crane Gear Damage. *Eng. Fail. Anal.* **115**, 104613 (2020). <https://doi.org/10.1016/j.engfailanal.2020.104613>
13. J. Pedrero, M. Pleguezuelos, M. Muñoz, Critical stress and load conditions for pitting calculations of involute spur and helical gear teeth. *Mech. Mach. Theory.* **46**, 425–437 (2011). <https://doi.org/10.1016/j.mechmachtheory.2010.12.001>
14. G. Metra, M. Somani, N. Babu, T.T. Watts, Contact stress analysis on composite spur gear using finite element method. *Mater. Today Proc.* **5**, 13585–13592 (2018). <https://doi.org/10.1016/j.matpr.2018.02.354>
15. X.F. Qin, R. Pang, X.G. Zhao, F. Li, Fracture failure analysis of internal teeth of ring gear used in reducer of coal mining machine. *Eng. Fail. Anal.* **84**, 70–76 (2018). <https://doi.org/10.1016/j.engfailanal.2017.08.022>
16. X.F. Qin, J. Liu, X.G. Zhao, F. Li, R.Q. Pang, Fracture failure analysis of transmission gear shaft in a bidirectional gear pump. *Eng. Fail. Anal.* **118**, 104886 (2020). <https://doi.org/10.1016/j.engfailanal.2020.104886>
17. W. Muhammad, K.M. Deen, Failure analysis of water pump shaft. *J. Fail. Anal. and Preven.* **10**, 161–166 (2010). <https://doi.org/10.1007/s11668-010-9332-0>
18. Z.L. Gao, B.Q. Huo, J.J. Zhang, Z.N. Jiang, Failure investigation of gear teeth fracture of seawater pump in a diesel engine. *Eng. Fail. Anal.* **105**, 1079–1092 (2019). <https://doi.org/10.1016/j.engfailanal.2019.07.050>
19. B. James, A. Hudgins, Handbook of materials failure analysis with case studies from the oil and gas industry. ISBN: 9780081001172. Chapter 1, pp. 33–36, Chapter 3, pp. 56–60

20. L.E. Spievak, P.A. Wawrzynek, A.R. Ingraffea, D.G. Lewicki, Simulating fatigue crack growth in spiral bevel gears. *Eng. Fract. Mech.* **68**, 53–76 (2001). [https://doi.org/10.1016/S0013-7944\(00\)00089-8](https://doi.org/10.1016/S0013-7944(00)00089-8)
21. M. Fonte, L. Reis, F. Romeiro, B. Li, M. Freitas, The effect of steady torsion on fatigue crack growth in shafts. *Int. J. Fatigue.* **28**, 609–617 (2006). <https://doi.org/10.1016/j.ijfatigue.2005.06.051>
22. J.R. Yates, M. Zanganeh, R.A. Tomlinson, M.W. Brown, F.A. Diaz Garrido, Crack paths under mixed mode loading. *Eng. Fract. Mech.* **75**, 319–330 (2008). <https://doi.org/10.1016/j.engfracmech.2007.05.014>
23. D.X. Jiang, C. Liu, Crack growth prediction of the steam turbine generator shaft. In *9th International Conference on Damage Assessment of Structures, (DAMAS2011)*. St Anne's College, University of Oxford, IOP, July 2011. (2011) pp. 11–13. <https://doi.org/10.1088/1742-6596/305/1/012023>
24. L.K. Ge, C.Q. Yuan, Z.W. Guo, X.P. Yan, Prediction and evaluation of cracks on thrust shaft. In *The 3rd International Conference on Transportation Information and Safety, (Wuhan), IEEE*, June 25–28, (2015) pp. 861–864. <https://doi.org/10.1109/ICTIS.2015.7232153>.
25. F. Cura, A. Mura, C. Rosso, Crack propagation behavior in planet gears. In *21st European Conference on Fracture, (Catania). Structural Integrity Procedia, ECF21*, 20–24 June 2016, pp. 3610–3616. <https://doi.org/10.1016/j.prostr.2016.06.450>.
26. K. Suga, M. Kikuchi, Y. Wada, H. Kawai, Study on fatigue growth of multi-surface flaws in shaft under rotary bending by S-FEM. *Eng. Fract. Mech.* **174**, 207–214 (2017). <https://doi.org/10.1016/j.engfracmech.2016.11.001>
27. P. Rubio, J. Bernal, L. Rubio, B. Muñoz-Abella, Study of the propagation of concave semi-elliptical shaped breathing cracks in rotating shafts. *Int. J. Fatigue.* **129**, 105214 (2019). <https://doi.org/10.1016/j.ijfatigue.2019.105214>
28. A. Soloba, A. Grbovića, Ž Božićb, S.A. Sedmakk, XFEM based analysis of fatigue crack growth in damaged wing-fuselage attachment lug. *Eng. Fail. Anal.* **11**, 1–9 (2020). <https://doi.org/10.1016/j.engfailanal.2020.104516>
29. H.W. Ye, Z.C. Duan, S.Q. Tang et al., Fatigue crack growth and interaction of bridge wire with multiple surface cracks. *Eng. Fail. Anal.* **116**, 104739 (2020). <https://doi.org/10.1016/j.engfailanal.2020.104739>
30. Y.H. Dong, X.F. He, X.N. Sun et al., Fatigue crack growth of a corner crack at the edge of a hole. *Int. J. Fatigue.* **139**, 105699 (2020). <https://doi.org/10.1016/j.ijfatigue.2020.105699>
31. R. Langloisa, R. Cusset et al., Multi-partner benchmark experiment of fatigue crack growth measurements. *J. Eng. Fract. Mech.* **235**, 107157 (2020). <https://doi.org/10.1016/j.engfracmech.2020.107157>
32. M. Fossati, M. Pagani, M. Giglio et al., Fatigue crack propagation in a helicopter component subjected to impact damage. *Def. Technol.* **2**(5), 1–13 (2020). <https://doi.org/10.1016/j.dt.2020.02.005>
33. A.R. Maligno, S. Rajaratnam, S.B. Leen et al., A three-dimensional (3D) numerical study of fatigue crack growth using remeshing techniques. *Eng. Fract. Mech.* **77**, 94–111 (2010). <https://doi.org/10.1016/j.engfracmech.2009.09.017>
34. M.C. Baietto, E. Pierres, A. Gravouil et al., Fretting fatigue crack growth simulation based on a combined experimental and XFEM strategy. *Int. J. Fatigue.* **47**, 31–43 (2013). <https://doi.org/10.1016/j.ijfatigue.2012.07.007>
35. P.C. Paris, F. Erdogan, A critical analysis of crack propagation laws. *J. Basic Eng.* **85**, 528–553 (1963)
36. F. Ergodan, G.C. Sih, On the crack extension in plates under plane loading and transverse shear. *J. Basic Eng.* **85**, 519–525 (1963)
37. D. Zhang, P. D. Zhong, C.H. Tao, Z.S. Lei, *Failure Analysis* (National Defense Industry Press, Beijing, 2013), pp. 54–62.
38. H.A. Richard, M. Sander, *Fatigue Crack Growth: Detect-Assess-Avoid* (Springer International Publishing, 2016), pp. 113–151. <https://doi.org/10.1007/978-3-319-32534-7>
39. S. Glodez, S. Pehan, J. Flaker, Experimental results of the fatigue crack growth in a gear tooth root. *Int. J. Fatigue.* **20**(9), 669–675 (1998). [https://doi.org/10.1016/S0142-1123\(98\)00040-1](https://doi.org/10.1016/S0142-1123(98)00040-1)
40. AGMA standards. (<http://www.agma.org/>)

**Publisher's Note** Springer Nature remains neutral with regard to jurisdictional claims in published maps and institutional affiliations.

Springer Nature or its licensor (e.g. a society or other partner) holds exclusive rights to this article under a publishing agreement with the author(s) or other rightsholder(s); author self-archiving of the accepted manuscript version of this article is solely governed by the terms of such publishing agreement and applicable law.